# Microsphere-assisted phase-shifting profilometry

**Stephane Perrin**[1,*], **Audrey Leong-Hoï**[1], **Sylvain Lecler**[1], **Pierre Pfeiffer**[1], **Ivan Kassamakov**[2], **Anton Nolvi**[2], **Edward Hæggström**[2], and **Paul Montgomery**[1]

[1] *ICube, University of Strasbourg - CNRS, 300 Boulevard Sebastien Brant, ILLKIRCH, France*
[2] *University of Helsinki, Gustaf Hällströmin katu 2, HELSINKI, Finland*
[*] *Corresponding author: stephane.perrin@unistra.fr*

---

**In the present work, we have investigated the combination of super-resolution microsphere-assisted 2D imaging technique with low-coherence phase-shifting interference microscopy. The imaging performance of this technique is studied by numerical simulation in terms of the magnification and the lateral resolution as a function of the geometrical and optical parameters. The results of simulations are compared with the experimental measurements of reference gratings using a Linnik interference configuration. Additional measurements are also shown on nanostructures. An improvement by a factor of 4.7 in the lateral resolution is demonstrated in air, thus giving a more isotropic nanometric accuracy for full-field surface profilometry in the far field.**

---

## 1. INTRODUCTION

White-light interference microscopy has become a standard method for the measurement of microscopic surface roughness and surface topography [1]. Based on optical imaging and interferometry, the technique has the advantages of being rapid and having a very high axial sensitivity i.e., $\sim 10$ nm (coherence scanning interferometry) to sub-nm (phase shifting interferometry), over a high depth of field [2]. However, despite a large field of view (FOV), the lateral resolution $\delta_{x,y}$ is limited by the diffraction from the microscope objective. In classical incoherent imaging, this is defined as the ratio between the central wavelength of the light source $\lambda_0$ and the numerical aperture (NA), multiplied by a factor $\kappa$ depending on the coherence of the light source and on the criterion used. By decreasing the wavelength or increasing the NA, a better lateral resolution can thus be achieved. According to the Fourier optics criterion ($\kappa = 0.5$) [3], the resolution cannot be greater than $\lambda/2$ in air. Nevertheless, in the visible range, the non-uniform resolution of interference microscopy remains i.e., the lateral resolution is over two orders of magnitude worse than the axial sensitivity [4].

Many methods have been developed over the last two decades in order to overcome the optical barrier of diffraction and thus to perform far-field optical nanoscale imaging and measurements. Some of the main principles of label-free far-field nanoscopy for materials characterization were studied at the beginning of the 1990's, demonstrating how nanostructures and details could be observed, measured, and studied in the far field [5–7]. In a later review of optical nanoscopy methods, we

highlighted the difference between nano-detection and super-resolution techniques [8]. Optical nanoscopy was then brought to the forefront with the Nobel Prize for Chemistry in 2014 for two new techniques in high-resolution fluorescence microscopy [9]. The first one involved the nano-detection of fluorescent marker molecules in photoactivated localization microscopy [10] and stochastic optical reconstruction microscopy [11]. The nanometric positioning of these markers allows the reconstruction of nanostructures without directly resolving the features optically. In contrast, the second technique, stimulated emission depletion microscopy [12], is based on super-resolution, with a real improved lateral resolution. Although the lateral resolution achieved is several tens of nm, the need for high light intensities can nonetheless be destructive to living matter. Other 2D super-resolution methods exist, such as 4Pi illumination [13], scattering lens microscopy [14], the far-field superlens, the Pendry hyperlens [15] and submerged microsphere optical nanoscopy [16]. Those that have been developed specifically for 3D measurement include structured illumination microscopy [17] and tomographic diffraction microscopy [18, 19], both of which generate a larger synthetic numerical aperture.

In 2004, the photonic jet was introduced as a non-classical phenomenon resulting from the sub-diffraction focusing properties of transparent microspheres [20, 21]. This effect of a reduced spot size was then used to improve the lateral resolution in a super-resolution scanning imaging technique [21, 22]. In 2011, Wang *et al.* demonstrated experimentally the principle of microsphere-assisted super-resolution imaging in a full-field configuration and far-field detection without the need for sam-

ple labelling [23]. Illuminated by a white-light source, a glass microsphere was placed on the sample. Then, a classical microscope objective, placed above the microsphere, collects the magnified virtual image of the sample. A lateral resolution of 50 nm is claimed, although this is actually half of the value for $\delta_{x,y}$ according to the Fourier optics criterion. In order to perform non-invasive acquisitions, recent work has shown that the microsphere can also be placed in a contactless configuration with the object while keeping the super-resolution [24]. Furthermore, in 2016, Wang *et al.* developed the first microsphere-assisted super-resolution microscope based on the coherence scanning interferometry [25]. By placing a BaTiO$_3$ microsphere in water in the object arm of a Linnik interferometer, a lateral resolution of 60 nm is claimed. At the same time, Kassamakov *et al.* proposed the use of a microsphere in a Mirau configuration in air to provide higher lateral resolution 3D surface measurements [26]. The microsphere-assisted technique was then applied to digital holography for precise cell identification [27].

In this work, we present results of the first microsphere-assisted phase-shifting (MAPS) Linnik-based nanoscopy system, in air, using low-coherence illumination. Taking advantage of the low-coherent noise of white-light illumination [28], and of the low frame number and of the high axial sensitivity of phase-shifting microscopy [1], the surface topography of samples is measured with much higher lateral resolution than in classical interferometry. First, the principle of lateral super-resolution has been investigated by numerical analysis through 2D finite element method simulations. Second, low-coherent phase-shifted measurements using a Linnik configuration and glass microspheres in air have been made and compared with the numerical results in terms of the magnification and the resolution provided by the microsphere. The MAPS technique consists of the five-step algorithm with a vertical displacement of the object. By measuring through 25-μm diameter glass microspheres, the 3D reconstruction of square profile gratings is achieved with a higher lateral resolution than with the objective alone. Reconstructions of 2-μm, 800-nm and 400-nm period gratings are shown using the MAPS system and a standard Linnik interferometer. An improvement by a factor of 4.7 in the lateral resolution is demonstrated in air.

Figure 1 shows an example of the direct imaging (2D imaging) of a 800-nm period grating using the microsphere-assisted microscopy. The features of the sample are not visible using the collecting objective (×50, NA = 0.3) in air alone (Fig.1(a)), unlike using a soda lime silica glass microsphere (Fig.1(b)). In this manuscript, 25-μm diameter glass microspheres were retained in order to perform a good compromise between magnification, lateral resolution improvement, field-of-view, and image plan position.
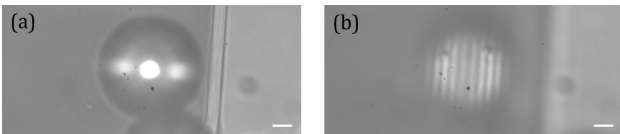


**Fig. 1.** Direct imaging of a 800-nm period grating using (a) a microscope objective (×50, NA = 0.3) alone and (b) the microsphere-assisted microscopy where the microsphere diameter is 25 μm. The central wavelength of the light source is 820 nm. White scale bars represent 4 μm.

## 2. SIMULATION

The phenomenon of microsphere-assisted microscopy has been numerically analysed in two dimensions in air [26] for confirming the experimental measurements. The rigorous electromagnetic simulation has been performed using Comsol Multyphysics finite element software. The size of the area studied is 30 × 30 μm² and is surrounded by perfectly matched layers. The maximum mesh size is $\lambda/10$ with $\lambda$, the wavelength of the light. The diameter $D$ of the soda lime silica glass microsphere equals 25 μm and its refractive index $n$ is wavelength-dependent [29]. Two spatially and temporally coherent point sources A and B are placed underneath the microsphere, as shown in Fig.2, and are spaced by a known distance $\overline{AB}$. The electromagnetic waves emitted by both A and B are first propagated into the microsphere.
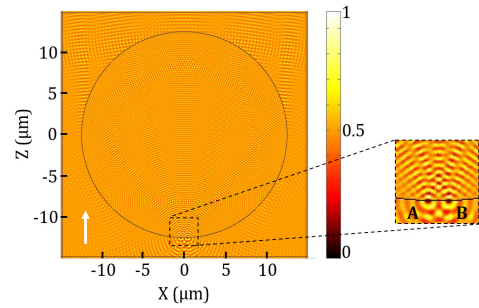


**Fig. 2.** Normalized real part of the electric fields from A and B propagated through a 25-μm diameter soda lime silica glass microsphere in air ($\lambda$ = 400 nm, $n$ = 1.53) for $\overline{AB}$ = 800 nm. The white arrow indicates the direction of the electric-field propagation.

In order to retrieve the image, which in this particular case is virtual, the complex electric field above the microsphere is therefore time-reversed propagated as shown in Fig.3.
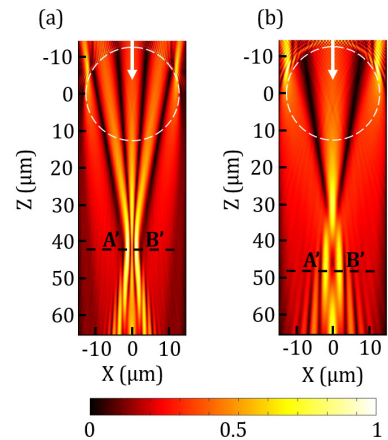


**Fig. 3.** Normalized amplitude of the back-propagated electric field in free space when the wavelength equals (a) 400 nm ($n$ = 1.53) and (b) 800 nm ($n$ = 1.51). The dotted black line represents the imaging plane. The white arrows indicate the direction of the electric-field propagation. The microsphere is represented by a dotted white circle only to illustrate its position (but is not used for the back-propagation calculation).

This is performed in free space i.e., in the absence of the mi-

crosphere, and in the opposite Z direction. The virtual images A′ and B′ of the objects then correspond to the X and Z positions of the maximal intensities. The value along Z gives the position of the virtual image plane (represented by the dotted black lines in Fig.3) and the distance $\overline{A'B'}$ between the two maximal intensities along the X axis leads to the magnification. The performance of the microsphere in terms of the magnification and the lateral resolution have been evaluated as a function of the wavelength $\lambda$ of the light source, and the diameter $D$. Due to the large number of parameters tested, we report only the numerical results related to the experiments.

First, the magnification provided by the microsphere, defined as the ratio between $\overline{A'B'}$ and $\overline{AB}$, was simulated as a function of the wavelength of the visible light source, with the resulting curve given in Fig.4. These first simulation results show that the magnification depends on the wavelength and, in the case considered, increases as a function of the wavelength. Indeed, the higher is the wavelength, the further is the imaging plane from the microsphere and the greater is $\overline{A'B'}$ (see results in Fig.3). However, for wavelengths higher than 800 nm, the magnification tends towards a constant value of around 4.8. For wavelengths of 500 nm and 850 nm, the magnification equals 3.5 and 4.5, respectively.
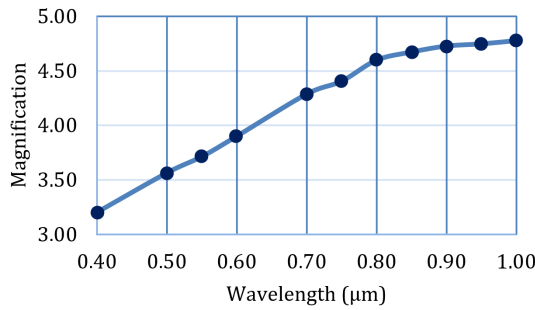


**Fig. 4.** Magnification of the object generated by the microsphere as a function of the wavelength.

In the second series of simulations, the full width at half maximum (FWHM) of the smallest discernible object by the microsphere has been estimated i.e., following the Houston criterion for a circular pupil ($\kappa \sim 0.5$) [30]. This value is defined as the ratio between the FWHM of the virtual image of a point source i.e., the point spread function (PSF), and the magnification [31]. The evolution of the FWHM as a function of the wavelength is shown in Fig.5.
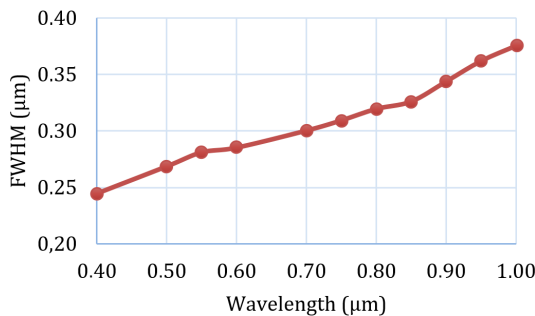


**Fig. 5.** FWHM in the object plane as a function of the wavelength.

Despite higher magnification values for longer wavelengths, the FWHM continues to increase with the wavelength, which means that higher magnification does not imply better resolution. In the case presented in Fig.4, the lateral resolution obtained using a 25-µm diameter microsphere reaches 270 nm at $\lambda$ = 500 nm. It should be noted that, without the microsphere and using a coherent illumination at $\lambda$ = 500 nm, an appropriate microscope objective (NA = 0.55) alone can only resolve structures larger than 900 nm. Indeed, an imaging system illuminated by a coherent light source provides a resolution of $\delta_{x,y} = \lambda/NA$ i.e., $\kappa = 1$ [3]. Thus, in this case, it is shown that the microsphere-assisted imaging technique improves the lateral resolution by a factor of 3.3 i.e., in the absence of the microsphere, a microscope objective would require a NA of 1.85 to achieve an equivalent lateral resolution.

Further simulations of this nature have shown that a FWHM of 70 nm ($\lambda/6$) can be obtained by using a microsphere with a diameter of 5 µm and a refractive index of 1.9, immersed in water, with coherent illumination at a wavelength of 400 nm. In air, the FWHM decreases to 100 nm ($\lambda/4$). For such a small diameter of microsphere, combined with spherical aberrations, the usable lateral FOV is reduced to a value of around 1 µm.

For clarity, the numerical analysis of the super-resolution performance described previously has been performed using a single wavelength. Because in the experiments, a white-light source was used to avoid coherent noise [28], the simulation was then repeated by considering the full spectral band of the illumination ($\lambda_0$ = 820 nm and $\Delta\lambda \sim$ 500 nm). The determination of the FWHM of the PSF of the microsphere in this case results in a value of 320 nm in air.

## 3. EXPERIMENTAL METHOD

A MAPS system based on a Linnik configuration has been used for the experimental measurements (Fig.6).
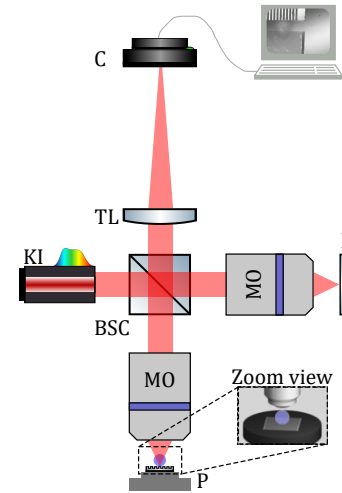


**Fig. 6.** General layout of the experimental setup based on a Linnik configuration, consisting of a broadband Köhler illumination system KI, a beam-splitter cube BSC, two ×50 microscope objectives MO, a reference mirror M, a tube lens TL and a camera C. A piezo-electric device P supports the sample on which the microsphere is placed (blue).

The incident beam from the broadband Köhler illumination (KI) is divided into two by the beam-splitter cube (BSC). The

transmitted beam i.e., the reference beam, passes through a ×50 microscope objective (MO) and is then reflected by the reference mirror (M). The reflected beam i.e., the object beam, passes through a similar MO and a microsphere which is placed manually using a fine mechanical tip on the sample in front of the objective (zoom view in Fig.6). The NA of the MO's was calibrated and determined to be 0.3. The diameter of the soda lime silica glass microsphere is similar to that simulated previously ($D$ = 25 μm). The MO collects the virtual image of the sample generated by the microsphere (as in Fig.1(b)) and the BSC combines both the object and reference beams.

The position of the components of the reference arm is then adjusted to balance the two arms of the interferometer due to the presence of the microsphere. When the optical path difference (OPD) between the two arms is inferior to the coherence length of the light source, an interference pattern occurs and is imaged on the camera (C) through the tube lens (TL). To improve the contrast of the interference fringes, the aperture diaphragm of the KI was reduced [25]. The piezo-electric device (P) supporting the sample allows a variation in the OPD to implement the standard five-step phase-shifting technique [1]. Therefore, five phase-shifted interference patterns with a phase-shifting step of $\pi/2$ are recorded and the phase distribution $\phi$(x,y) is retrieved using the following equation:

$$\phi\left(x,y\right) = \arctan\left[\frac{2\left(I_2 - I_4\right)}{2I_3 - I_5 - I_1}\right],\qquad (1)$$

where $I_1$, $I_2$, $I_3$, $I_4$ and $I_5$ are the five frames with 0, $\pi/2$, $\pi$, $3\pi/2$ and $2\pi$ phase shifts, respectively. Post-processing of each image is implemented, consisting of a median filter to reduce noise. In order to remove the phase jumps of $2\pi$ resulting from the arctangent function, an unwrapping algorithm based on a non-iterative method [32] was developed and the OPD was then evaluated. In classical interferometry, the phase $\phi$(x,y) and the OPD are linked by the following equation:

$$\phi\left(x,y\right) = 2\pi\frac{OPD\left(x,y\right)}{\lambda}\qquad (2)$$

With $\lambda$, the effective wavelength of the light source. Then, the topography of the sample is estimated by considering the refractive index variations in both object and reference arms. However, in the MAPS technique, a microsphere is placed in the object arm, adding a non-uniform optical path distribution due to its spherical shape. The term OPD rather than height has thus been retained in order to avoid confusion.

The measurements have been performed using two types of light source i.e., a incandescent lamp and a white-light LED having central wavelengths $\lambda_0$ of 820 nm and 560 nm, respectively. Without implementation of the MAPS technique, the lateral resolution $\delta_{x,y}$ of the MO is 1.3 μm for $\lambda_0$ = 820 nm and 900 nm for $\lambda_0$ = 560 nm.

## 4. RESULTS AND DISCUSSION

To validate the MAPS technique, calibrated standard gratings from SiMETRICS GmbH with a period of $\Lambda$ = 2 μm, $\Lambda$ = 800 nm and $\Lambda$ = 400 nm, were measured and the results of the surface topography were compared with those using a Park XE 70 atomic force microscope (AFM). The lateral resolution limitation from the MAPS technique is achieved when $\Lambda$ = 800 nm ($\sim 2\times$FWHM, for $\lambda_0$ = 820 nm) and when $\Lambda$ = 400 nm ($\sim 2\times$FWHM, for $\lambda_0$ = 560 nm).

Figure 7 shows the topography measurements of the 2-μm

period grating. Four microspheres were placed on the sample, as can be seen in the direct image (in Fig.7(a)), in the interference pattern (in Fig.7(b)) and in the phase reconstruction (in Fig.7(c)). However, only the left-bottom microsphere was used to reconstruct the three-dimensional topography in Fig.7(d). The results from the three other microspheres were not considered.
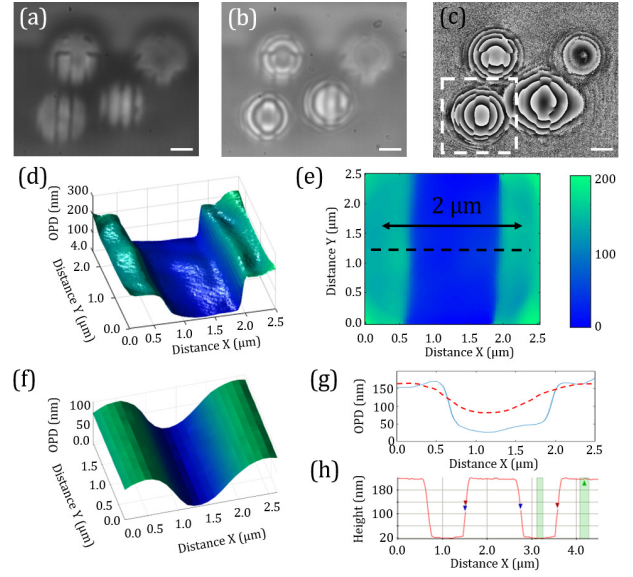


**Fig. 7.** Measurement results of the topography of the 2-μm pitch grating through a 25-μm diameter glass microsphere illuminated by the incandescent lamp: (a) the direct image, (b) the interference pattern, (c) the wrapped phase though 4 microspheres. White dotted rectangular is the region of interest used for (d) the 3D reconstruction of (e) the topographic surface from the left-bottom microsphere. (f) The topographic surface is also measured through the MO alone. (g) The cross-section height profiles without microsphere (red dotted line) and with microsphere (blue solid line) can be compared with (h) those obtained using AFM (average height = 180 nm). White scale bars represent 2 μm.

Assuming a period of 2 μm as having being measured, the microsphere provides an additional magnification of 4.5, as expected in the simulations (see Fig.4 at $\lambda$ = 820 nm). The average OPD between the top and bottom of the groove is about 150 nm, slightly less than the value of 190 nm found by AFM and the quoted value of 194 nm (SiMETRICS). Indeed, the OPD in the MAPS technique includes the height distribution of the sample as well as other terms, of which the refractive index of the microsphere. This could explain the slight height difference between both the measured and the expected depths. Moreover, as is explained in the following sections, due to the spherical and chromatic aberrations, the shape of the measured edge (see Fig.7(e)) as well as the cross-sectional profile (see Fig.7(g)) are deformed. Nevertheless, the resolution of the interferometer using the MAPS technique is higher than that without the microsphere (see Fig.7(f)) i.e., the height value is 60 nm using the MO alone (see Fig.7(g)).

The results of the 800-nm period grating are shown in Fig.8. Assuming a period of 800 nm as having been measured, the additional magnification is also 4.5, corresponding to the simulation results. In the numerical analysis, for $\lambda_0$ = 820 nm, the FWHM of the discernible object is estimated to be 320 nm ($\sim \Lambda/2$).
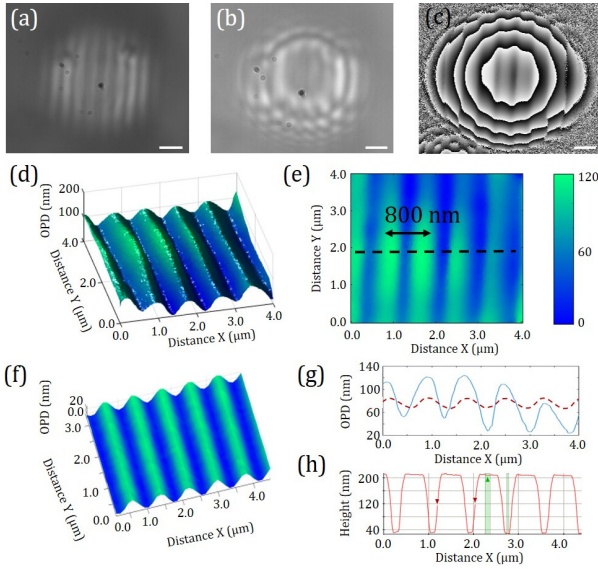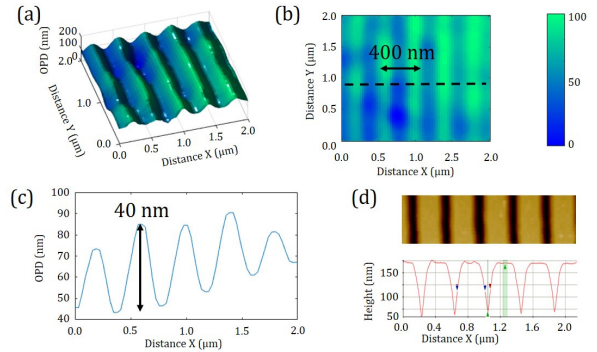
**Fig. 8.** Measurement results of the topography of the 800-nm pitch grating through a 25-μm diameter glass microsphere illuminated by the incandescent lamp: (a) the direct image, (b) the interference pattern, (c) the wrapped phase, (d) the 3D reconstruction of (e) the topography surface through the microsphere, and (f) the topographic surface through the MO alone. (g) The cross-section height profiles without the microsphere (red dotted line) and with microsphere (blue solid line) can be compared with (h) those obtained using AFM (average height = 180 nm). White scale bars represent 1 μm.

The average OPD between the top and bottom of the grooves is about 110 nm, smaller than the value of 180 nm found by AFM (Fig.8(h)) and the quoted value of 180 nm (SiMETRICS). This latter result could be explained by the difference between the OPD and real height value as explained previously. Furthermore, the size of the half of the grating period in the virtual plane ($4.5 \times \Lambda / 2 = 1.8$ μm) is higher than the lateral resolution limit of the MO ($\delta_{x,y} = 1.3$ μm). Moreover, in Fig.8(b) the contribution of the +1 and -1 diffraction order of the grating can also be observed, which could alter the measurement on the border for this kind of sample. However, the interferometer assisted by a microsphere provides a higher resolution than without the microsphere (average height = 20 nm) and thus a higher axial dynamic range as shown in Fig.8(g)), the comparison of the height profiles.

To improve the results, the incandescent source was replaced by a white-light LED which has a smaller central wavelength ($\lambda_0 = 560$ nm). The results of measurements through the microsphere of a grating with a period of 400 nm are presented in Fig.9. The experimental magnification is 3.5 which is equivalent to that found by simulation. The lateral resolution is thus improved by a factor of 4.7 ($\sim \delta_{x,y} \times 2 / \Lambda$). While the imaging system can distinguish the grating pattern, the average OPD between the top and bottom of the grooves is about 40 nm, much less than the height value of 90 nm found by AFM (Fig.9(d)). As mentioned previously, the error in the height measurement could be due to the difference between the OPD and real height value and/or to the fact that the lateral resolution limit of the MO is reached ($\delta_{x,y} = 900$ nm $\sim 3.5 \times \Lambda/2$). In this case, the FWHM due to the microsphere is 270 nm ($\sim \Lambda/2$). Moreover, the groove appears as a "V" shape in the AFM measurement

(Fig.9(d)) which could be due to the convolution of the tip shape with the straight groove, leading to a wrong interpretation of the axial accuracy.



**Fig. 9.** Measurement results of the topography of the 400-nm pitch grating through a 25-μm diameter glass microsphere illuminated by a white-light LED: (a) the 3D reconstruction of (b) the topography surface and (c) the profile of the black dotted line in (b). This result can be compared with (d) obtained using AFM (average height = 90 nm).

A second type of sample was then measured using the microsphere consisting of a series of Ag nano-dots covered by a SiON layer on a Si wafer made by nano imprint lithography. The periodical elliptical nanostructures have an approximate size of 200 nm × 300 nm, and are separated by 200 nm and 300 nm along the X and Y axes respectively. The average height is 28 nm. The measurements of the topography made through the 25-μm microsphere are shown in Fig.10.
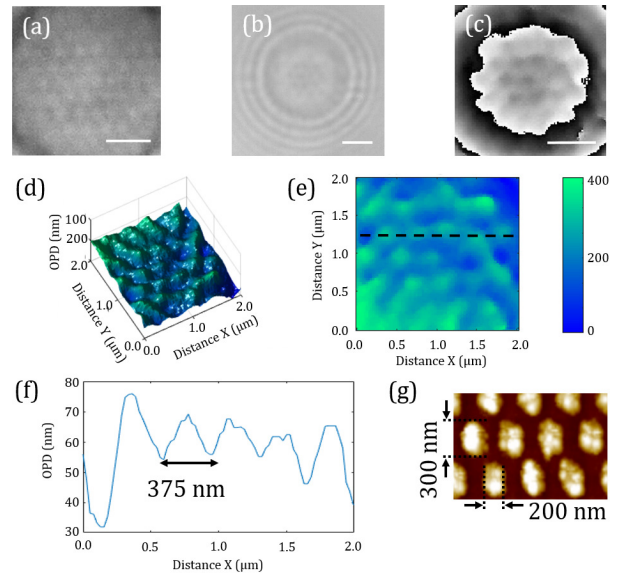


**Fig. 10.** Measurement results of the topography of oval-shaped nano particles of Ag covered by a SiON layer through a 25-μm diameter glass microsphere illuminated by the white-light LED: (a) the direct image, (b) the interference pattern, (c) the wrapped phase, (d) the 3D reconstruction of (e) the topography surface and (f) the profile of the black dotted line in (e). This result can be compared with (g) obtained using AFM (average height = 28 nm). White scale bars represent 1 μm.

The pattern of nano-elements was observable through both the direct image (Fig.9(a)) and the phase distribution (Fig.10(c)). Moreover, the OPD measurements of the heights of the structures with MAPS (Fig.10(d-f) are similar to the measurements using AFM (Fig.10(g)). While the acquisition time for the AFM measurements is 15 minutes (256 × 256 pixels) due to point scanning, the MAPS technique allows a full-field measurement of the nano-objects thanks to the microsphere in less than 10 seconds since it does not require lateral scanning. As shown in Fig.10(e), the OPD reconstruction is sloped. The next section explains the subsequent corrections performed.

## 5. WAVEFRONT-DEFORMATION CORRECTION

The use of a spherical microlens yields a curved deformation in the measured phase as shown in Fig.11.
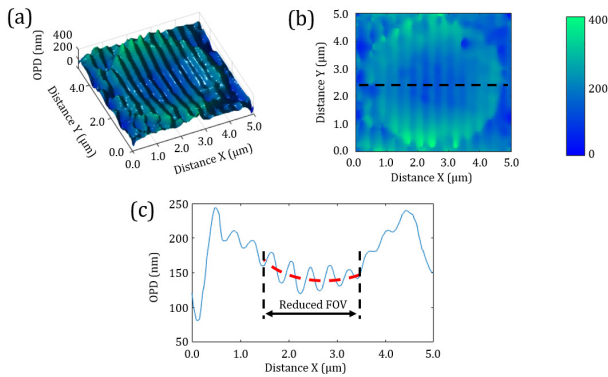


**Fig. 11.** Reconstruction of the topography of the 400-nm period grating through a 25-μm diameter glass microsphere illuminated by a white-light LED. The representation differs by its FOV (5 × 5 μm²) which is much larger than that used in Fig.9 (2 × 2 μm²).

If the FOV of the 400-nm period grating measurement is increased, the phase reconstruction can be seen to contain rings which are due to the non-negligible spherical aberrations typically generated by microspheres of this size [33]. In the previous measurements, assuming a flat sample, the aberration terms have been removed by reducing the FOV and then applying a polynomial 2D fit with a linear least squares method as shown in Fig.11(c) by the red dotted lines. Then, the residual approaches the wavefront free of the spherical aberration term.

## 6. CONCLUSION

The combination of a super-resolution microsphere-assisted imaging technique with low-coherence phase-shifting interference microscopy has been investigated. An experimental system based on a Linnik configuration has demonstrated an improvement by a factor of 4.7 in the lateral resolution in air. For a 25-μm diameter glass microsphere, a lateral resolution of 200 nm at a wavelength of 560 nm has been achieved with a microscope having a NA of 0.3, for an axial sensitivity of several nm. Without the microsphere, the interferometer would require an equivalent numerical aperture of 1.4 to achieve the same lateral resolution. High resolution 3D measurements have been performed on reference gratings and nanostructures. A more isotropic nanometric accuracy is thus achieved for full-field surface profilometry, with the advantages of being in the far field. The imaging performance has also been studied by numerical simulation in terms of the magnification and the lateral resolution as a function of the geometrical and optical parameters and confirm the experimental measurements. Using a microsphere combined with phase-shifting interferometry, this new 3D imaging technique appears to be very promising for nanometrology.

## FUNDING

## REFERENCES

1. D. Malacara, *Optical Shop Testing, 3rd Ed.* (Wiley, 2007).
2. P. de Groot, "Principles of interference microscopy for the measurement of surface topography," Adv. Opt. Photon. **7**, 1-65 (2015).
3. C. Williams and O. Becklund, *Introduction to the Optical Transfer Function* (Wiley Series in Pure and Applied Optics, 1989).
4. P. C. Montgomery and D. Montaner, "Deep submicron 3D surface metrology for 300 mm wafer characterization using UV coherence microscopy," Microelectron. Eng. **45**, 291 (1999).
5. P. C. Montgomery, "Nanometre defect analysis by computer aided 3D optical imaging," Nanotechnology **1**, 54 (1990).
6. J. P. Fillard, *Near Field Optics and Nanoscopy* (World Scientific, 1996).
7. S. W. Hell and J. Wichmann, "Breaking the diffraction resolution limit by stimulated emission: stimulated-emission-depletion fluorescence microscopy," Opt. Lett. **19**, 780 (1994).
8. P. C. Montgomery, A. Leong-Hoi, F. Anstotz, D. Mitev, L. Pramatarova, and O. Haeberle, "From superresolution to nano-detection: overview of far field optical nanoscopy techniques for nanostructure," JPCS **682**, 012010 (2016).
9. M. Ehrenberg, "Noble Price in Chemistry 2014," Press release (2014).
10. E. Betzig, G. H. Patterson, R. Sougrat, O. W. Lindwasser, S. Olenych, J. S. Bonifacino, M. W. Davidson, J. Lippincott-Schwartz, and H. F. Hess, "Imaging intracellular fluorescent proteins at nanometer resolution," Sciences **313**, 1642 (2006).
11. S. H. Shim, C. Xia, G. Zhong, H. P. Babcock, J. C. Vaughan, B. Huang, X. Wang, C. Xu, G. Q. Bi, and X. Zhuang, "Super-resolution fluorescence imaging of organelles in live cells with photoswitchable membrane probes," Proc. Natl. Acad. Sci. USA **109**, 13978 (2012).
12. T. A. Klar, S. Jakobs, M. Dyba, A. Egner, and S. W. Hell, "Fluorescence microscopy with diffraction resolution barrier broken by stimulated emission," PNAS **97**, 8206 (2000).
13. S. W. Hell, S. Lindek, C. Cremer, and E. H. K. Stelzer, "Confocal microscopy with an increased detection aperture: type-B 4Pi confocal microscopy," Opt. Lett. **19**, 222 (1994).
14. E. Van Putten, D. Akbulut, J. Bertolotti, W. Vos, A. Lagendijk, and A. Mosk, "Scattering Lens Resolves Sub-100 nm Structures with Visible Light," Phys. Rev. Lett. **106**, 193905 (2011).
15. J. B. Pendry, "Negative refraction makes a perfect lens," Phys. Rev. Lett. **85**, 18 (2000).
16. L. Li, W. Guo, Y. Yan, S. Lee, and T. Wang, "Label-free super-resolution imaging of adenoviruses by submerged microsphere optical nanoscopy," Light. Sci. Appl. **2**, e104 (2013).
17. M. G. Gustafsson, "Nonlinear structured-illumination microscopy: wide-field fluorescence imaging with theoretically unlimited resolution," Proc. Natl. Acad. Sci. USA **02**, 13081 (2005).
18. H. Liu, J. Bailleul, B. Simon, M. Debailleul, B. Colicchio, and O. Haeberlé, "Tomographic diffractive microscopy and multiview profilometry with flexible aberration correction," Appl. Opt. **53**, 748 (2014).
19. M. Debailleul, V. Georges, B. Simon, R. Morin, and O. Haeberlé, "High-resolution three-dimensional tomographic diffractive microscopy of transparent inorganic and biological samples," Opt. Lett. **34**, 79 (2009).
20. S. Lecler, Y. Takakura, and P. Meyrueis, "Properties of a three-dimensional photonic jet," Opt. Lett. **30**, 2641 (2005).

21. Z. Chen, A. Taflove, and V. Backman, "Photonic nanojet enhancement of backscattering of light by nanoparticles: a potential novel visible-light ultramicroscopy technique," Opt. Express **12**, 1214 (2004).
22. A. Heifetz, J. J. Simpson, S. C. Kong, A. Taflove, and V. Backman, "Subdiffraction optical resolution of a gold nanosphere located within the nanojet of a Mie-resonant dielectric microsphere," Opt. Express **15**, 17334 (2007).
23. Z. Wang, W. Guo, L. Li, B. Luk'yanchuk, A. Khan, Z. Liu, Z. Chen, and M. Hong, "Optical virtual imaging at 50 nm lateral resolution with a white-light nanoscope," Nat. Commun. **2**, 218 (2011).
24. F. Wang, L. Liu, H. Yu, Y. Wen, P. Yu, Z. Liu, Y. Wang, and W. J. Li, "Scanning superlens microscopy for non-invasive large field-of-view visible light nanoscale imaging," Nat. Commu. **7**, 13748 (2016).
25. F. Wang, L. Liu, P. Yu, Z. Liu, H. Yu, Y. Wang, and W. J. Li, "Three-dimensional super-resolution morphology by near-field assisted white-light interferometry," Sci. Rep., 24703 (2016).
26. I. Kassamakov, A. Nolvi, and E. Hæggström, "3D Super-resolution label-free imaging," in Conference on Lasers and Electro-Optics, OSA Technical Digest (OSA, 2016), paper AM4O.2
27. M. Aakhte, V. Abbasian, E. A. Akhlaghi, A. R. Moradi, A. Anand, and B. Javidi, "Microsphere-assisted super-resolved Mirau digital holographic microscopy for cell identification," Appl. Opt. **56**, D8 (2017).
28. P. Chavel, "Optical noise and temporal coherence," J. Opt. Soc. Am **70**, 935 (1980).
29. M. Rubin, "Optical properties of soda lime silica glasses," Sol. Energ. Mat. Sol **12**, 275-288 (1985).
30. W. V. Houston, "The Fine Structure and the Wave-Length of the Balmer Lines," APJ **64**, 81 (1926).
31. S. Perrin, A. Leong-Hoi, S. Lecler, and P.C. Montgomery "Role of coherence in microsphere assisted nanoscopy," Proc. SPIE **10330**, 1033033 (2017).
32. H. Takajo and T. Takahashi, "Noniterative method for obtaining the exact solution for the normal equation in least-squares phase estimation from the phase difference," J. Opt. Soc. Am. A **5**, 1818 (1988).
33. H. Guo, Y. Han, X. Weng, Y. Zhao, G. Sui, Y. Wang, and S. Zhuang, "Near-field focusing of the dielectric microsphere with wavelength scale radius," Opt. Express **21**, 2434 (2013).